

Giant Anisotropic in-Plane Thermal Conduction Induced by Anomalous Phonons in Pentagonal PdSe₂

Bin Wei^{1,2†*}, Junyan Liu^{2†}, Qingan Cai³, Ahmet Alatas⁴, Ayman H. said⁴, Meihua Hu¹, Chen Li^{3,5*}, Jiawang Hong^{2*}

¹Henan Key Laboratory of Materials on Deep-Earth Engineering, School of Materials Science and Engineering, Henan Polytechnic University, Jiaozuo 454000, China

²School of Aerospace Engineering, Beijing Institute of Technology, Beijing 100081, China

³Mechanical Engineering, University of California, Riverside, Riverside, CA 92521, USA.

⁴Advanced Photon Source, Argonne National Laboratory, Argonne, IL 60439, USA.

⁵Materials Science and Engineering, University of California, Riverside, Riverside, CA 92521, USA.

†The authors contribute equally

*Corresponding author: binwei@hpu.edu.cn; chenli@ucr.edu.cn; hongjw@bit.edu.cn

Abstract

In two-dimensional materials, different atomic stacking induces anisotropic atomic interactions and phonon dispersions, leading to the anisotropy of in-plane thermal transport. Here, we report an exceptional case in layered pentagonal PdSe₂, where the bonding, force constants, and lattice constants are nearly-equal along the in-plane crystallographic axis directions, while the thermal conductivity is surprisingly much greater along *b*-axis than along *a*-axis with a ratio up to 1.8. Such strong anisotropy is not only unexpected in in-plane uniform structured materials, but also

comparable to the record high in-plane anisotropic thermal conductivity in the nonuniform structured material reported to date (the ratio is ~ 2.0 in TiS_3). By combining the inelastic X-ray scattering measurement and the first-principles calculations, we attribute such high anisotropy to the low-energy phonons along a -axis, particularly their lower group velocities and “avoided-crossing” behavior. The different buckling structures between a - (zigzag-type) and b -axis (flat-type) are mainly responsible for such unique phonon dynamics properties of PdSe_2 . This finding helps to discover materials with high anisotropic in-plane thermal conductivity in uniform structures and reveals new physics of anisotropy of in-plane thermal conduction. Due to the unique features in structure and thermal transport properties, PdSe_2 may serve as a new platform for designing novel devices to route heat flow precisely at the nanoscale.

Keywords: anisotropy, thermal conductivity, phonon dispersion, inelastic X-ray scattering, PdSe_2

1. Introduction

Due to their excellent physical properties, low-dimensional materials play an irreplaceable role in meeting the requirements of intelligent and miniaturized devices. Potential applications of these materials have been studied in a variety of fields, such as electronics [1,2], sensors [3,4], and spintronics [5]. However, controlling heat dissipation remains a challenge, making thermal management an intriguing topic in optimizing the performance of the low-dimensional-materials-based devices. In two-dimensional (2D) layered materials, the weak interlayer van der Waals (vdW) interaction and the strong intralayer covalent bonds lead to highly anisotropic thermal conduction between the out-of-plane and in-plane directions. In addition, the anisotropy of in-plane thermal conductivity (IPTC) also exists in many 2D materia [6-9]. Such anisotropy is

mainly attributes to the different structures in the basal plane. Generally, the softer bonds will lead to lower thermal conductivity due to the lower phonon group velocity, while the harder bonds behave the opposite result [10-12]. For example, a record high anisotropy ratio of 2 has recently been reported in the basal plane of titanium trisulfide due to the large difference of bonding and lattice constants between *a*- and *b*-axis [9]. The thermal conductivity along the tightly bonded atomic chains (*b*-axis) shows twice as large as that along the weaker bonding interchain (*a*-axis) because the higher group velocity. In contrast, in the uniform honeycomb structure systems, such as graphene (lattice constant is 2.46 Å) [11], the IPTC is equal along the crystallographic axes, while in the basal plane, the IPTC is lower along armchair direction than zigzag direction due to the lower contribution from the localized phonon density of state, which will induce low phonon group velocity along armchair-direction. Furthermore, in structures with uniform bonds but with relatively large lattice constant ratio, such as honeycomb phosphorus with a lattice constant ratio of 0.71 [10,11], the IPTC has similar behavior as that of graphene along the zigzag and armchair directions. Therefore, even in relatively high symmetry in-plane structures with uniform bonds and equal lattice constants, the IPTC may show an anisotropic behavior if the phonon dispersions are different along the crystallographic axes. Yet, the strong IPTC anisotropy along the crystallographic axes in the uniform in-plane structure is rarely reported.

Recently, pentagonal-structure 2D materials, such as penta-graphene [13], penta-silicene [14], and noble metal dichalcogenides (MX_2) ($\text{M} = \text{Pt}, \text{Pd}$, and $\text{X} = \text{S}, \text{Se}, \text{Te}$) [15,16], have become the focus of interest due to their unique electrical, mechanical, and optical properties. Among them, palladium diselenide (PdSe_2) has been reported to show strong anisotropy of electrical [17,18], optical [15,17], and thermoelectric properties [19]. Much work has focused on the

theoretical lattice dynamics calculations, but less was confirmed by measurements [20- 22]. PdSe₂ takes a puckered pentagonal structure with an orthorhombic lattice ($a=5.75 \text{ \AA}$, $b=5.87 \text{ \AA}$, $c=7.69 \text{ \AA}$, $a/b=0.98$) (Fig. 1a) [23], in which four Se atoms covalently bond the Pd atom with a nearly-equal Pd-Se bond length ($2.44 \text{ \AA} / 2.44 \text{ \AA} \approx 1$), bond strength ($2.51 \text{ eV} / 2.50 \text{ eV} \approx 1$), and bond force constant ($4.18 \text{ eV \AA}^{-2} / 4.15 \text{ eV \AA}^{-2} \approx 1$) [24], showing a nearly-uniform structure along a - and b -axis (Fig. 1b). Surprisingly, a strong in-plane anisotropy of IPTC with a ratio up to 1.4 has recently been reported by micro-Raman thermometry (MRT) [22] in layered pentagonal PdSe₂. However, the in-plane lattice dynamics is still not explored experimentally and the microscopic mechanism of this strong thermal conductivity anisotropy is still unknown.

Here, we report a giant anisotropy of IPTC with a ratio up to ~ 1.8 in layered pentagonal PdSe₂ over a wide temperature range. Using the inelastic X-ray scattering (IXS) and the first-principles calculations, we find that such large anisotropic thermal conduction is closely related to the different buckling structures in PdSe₂. The puckered Se atoms make the [PdSe₄] planes form a zigzag-type chain along a -axis, which induces the flat low-energy (LE) phonon branch and the avoided-crossing behavior in the phonon spectrum, both of which strongly suppresses the heat transport. While the [PdSe₄] planes form a flat-type chain along b -axis, which induces more dispersive branches (higher group velocities), leading to higher thermal conductivity.

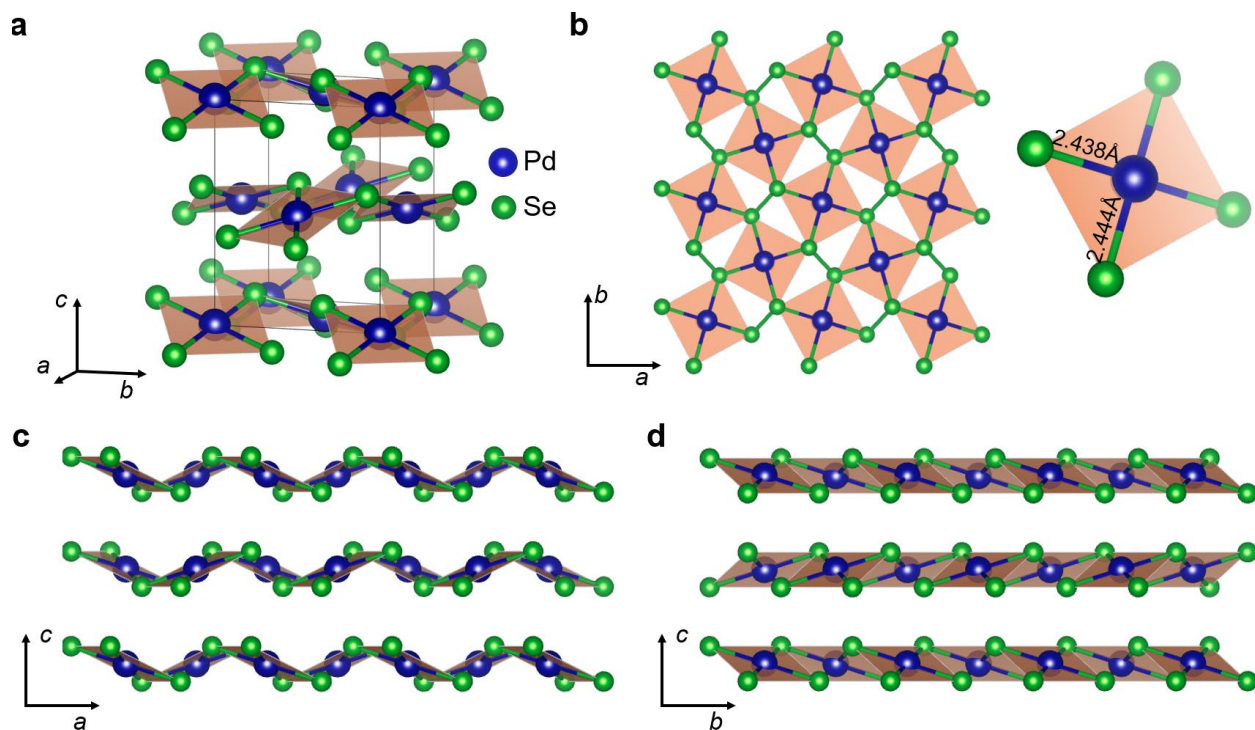


Fig. 1 Crystal structure of PdSe₂. **a** and **b** are the front and top views of the crystal structure, respectively. The nearly-equal Pd-Se bond lengths showing nearly-regular quadrilaterals. **c** and **d** are the side views, showing a zigzag-type pucker along *a*-axis and a flat-type pucker along *b*-axis, respectively.

2. Results and Discussion

The IXS measurements were obtained using the high-resolution inelastic X-ray (HERIX) spectrometer at the Advanced Photon Source (Supplementary Fig. 1, see Methods). Figure 2 shows the LE-phonon dispersions of PdSe₂ measured by IXS at room temperature along Γ -X, Γ -Y, and Γ -Z directions (*a*-, *b*-, and *c*-axis respectively in real space of orthorhombic structure), overlaid with the calculated dispersions (the entire energy dispersions are shown in Supplementary Fig. 2). It can be seen that the calculation is in excellent agreement with IXS measurements, particularly along the interlayer direction (vdW forces) (Fig. 2c). The accurate

modeling of the phonon dispersion is essential for the accuracy of the thermal conductivity calculations. The acoustic phonons along Γ -Z are much smaller than those in the basal plane, due to the interlayer vdW interactions being weaker than the intralayer covalent bondings.

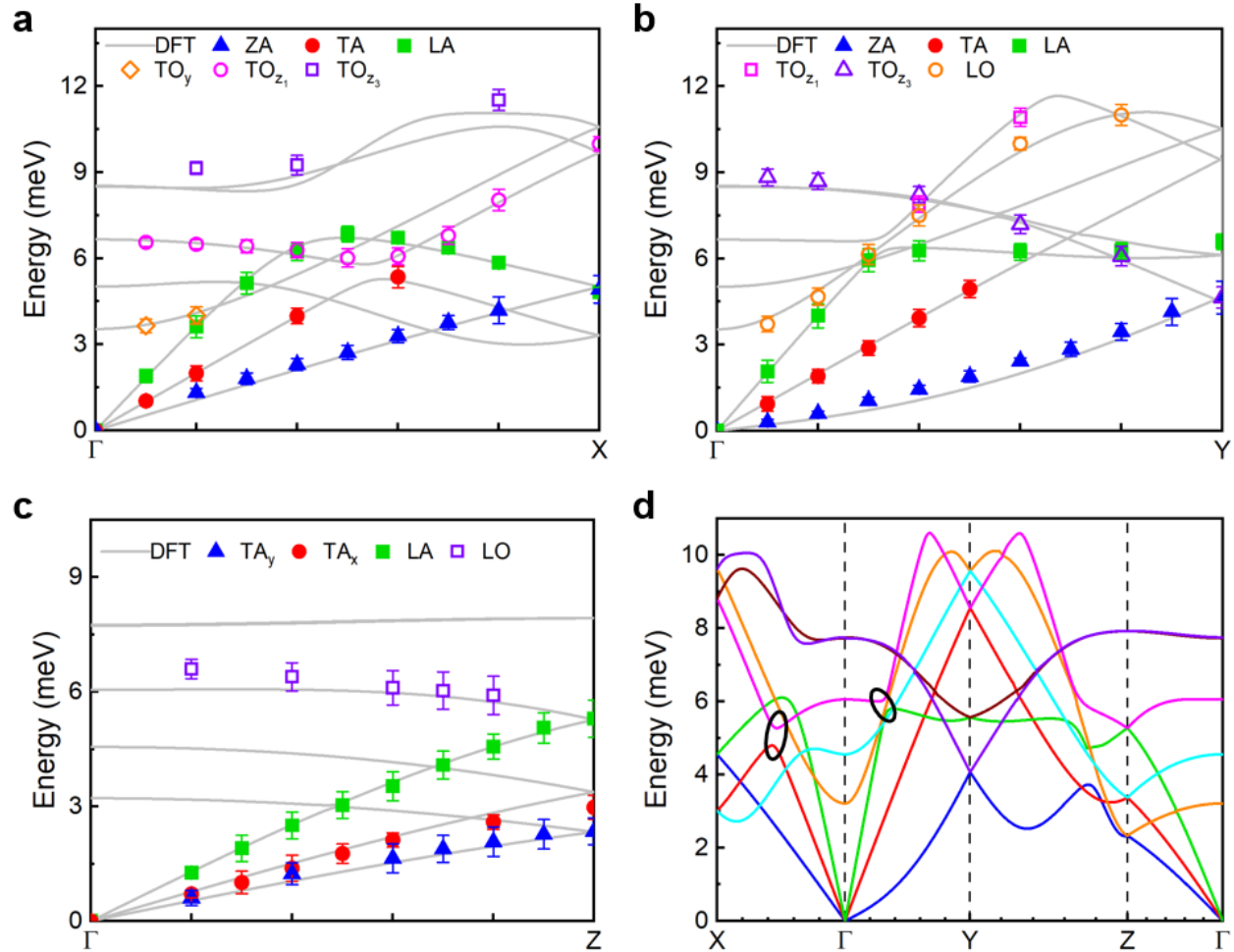


Fig. 2 Phonon dispersions of PdSe₂ measured at 300 K by inelastic X-ray scattering (IXS), overlaid with the first-principles calculations (DFT). **a**, **b**, and **c** are the dispersions along Γ -X, Γ -Y, and Γ -Z, respectively (shown as solid lines). Points are the measurements, and solid lines are the calculations. Blue triangle, red circle, green square, orange hollow diamond, magenta hollow circle, and purple hollow square represent the flexural acoustic (ZA) mode, transverse acoustic (TA) mode, longitudinal acoustic (LA) mode, transverse optical mode

vibrating along b -axis (TO_y), the first transverse optical mode vibrating along c -axis (TO_{z1}), and the third transverse optical mode vibrating along c -axis (TO_{z3}) in **a**. Blue triangle, red circle, green square, orange hollow circle, magenta hollow square, and purple hollow triangle represent the ZA, TA, LA, longitudinal optical (LO), TO_{z1} , and TO_{z3} modes in **b**. Blue triangle, red circle, green square, and purple hollow circle represent the transverse acoustic mode vibrating along b -axis (TA_y), transverse acoustic mode vibrating along a -axis (TA_x), LA mode, and LO mode in **c**. Error bars are the Gaussian fitting uncertainties. **d** Calculated low-energy phonon dispersions, sorted by the phonon eigenvector. Black ellipses indicate the avoided-crossing behavior.

Interestingly, the LE-phonon branches along Γ -X show significant differences from those along Γ -Y. For example, the flexural acoustic phonon (ZA) mode, a typical 2D materials featured mode [25] in which the atomic vibration along c -axis direction, shows an anomaly along a - and b -axis directions. ZA shows a linear dispersive curve along Γ -X, while it is quadratic along Γ -Y. Such behavior is quite different from that in other uniform 2D-layered (e.g., uniform pentagonal and hexagonal structures) and monolayered structures, where the ZA mode shows a quadratic-like curve in the basal plane [13,14,25,26]. This dispersive difference results from the buckling Se atoms in the zigzag- and flat-type chains (Figs. 1c and 1d), which form non-planar structures in the basal plane, leading to the non-pure out-of-plane vibration of the atoms (deviate from c -axis) near the zone center ($\mathbf{q} \rightarrow 0$) [27,28] (Supplementary Fig. 3 and Supplementary Table I). Thus, the ZA branches are not purely quadratic near Γ -point along Γ -X and possess nonzero group velocities [29]. In addition, the obvious avoided-crossing behavior [30,31] can also be seen from phonon dispersion both along a - and b -axis directions (black ellipses in Fig. 2d). The transverse acoustic (TA) branch along Γ -X is bent by the transverse optical mode vibrating

along c -axis (TO_{z1}) and ends only at 3 meV at X-point, while TA phonon along Γ -Y goes straightly up to 9 meV, without such avoided-crossing behavior. The longitudinal acoustic (LA) along Γ -Y also shows avoided-crossing behavior with the TO_{z1} mode. The second-lowest energy optical mode, identified as the longitudinal optical (LO) mode along Γ -X and TO_x mode along Γ -Y, exhibits a significant difference in slopes along the high-symmetry directions in the calculation. While the lowest energy optical mode, behaving as the TO_y mode along Γ -X and the LO mode along Γ -Y, also shows moderate difference in slopes along the high-symmetry directions.

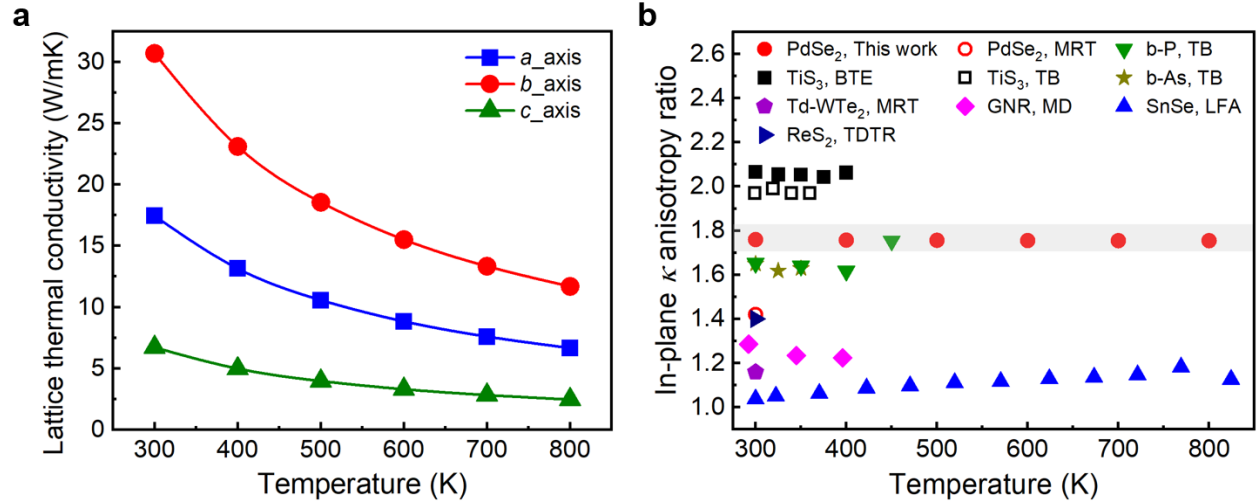


Fig. 3 Anisotropic thermal conductivity of PdSe₂. **a** Temperature-dependence of the anisotropic lattice thermal conductivity from the Boltzmann transport equation (BTE) calculations. **b** In-plane thermal conductivity anisotropy ratio of various 2D-layered materials versus temperature. The samples used for measurements are 1.62 nm thickness for PdSe₂ [22], 150 nm for ReS₂ [34], 11.2 nm for Td-WTe₂ [32], 100 nm for TiS₃ [9], 170 nm for b-P [7], bulk for SnSe [8], and 124 nm thick nanoribbon for b-As [33]. Abbreviations: Thermal bridge (TB), micro-Raman thermometry (MRT), graphene nanoribbon (GNR), molecular dynamics (MD),

laser flash apparatus (LFA), and time-domain thermoreflectance (TDTR). Grey shadow indicates the result of this work.

After obtaining the accurate phonon dispersions, we then calculated the thermal conductivity of PdSe₂. As shown in Fig. 3a, it can be found that out-of-plane thermal conductivity is the smallest one due to the weak vdW interaction. But surprisingly, the in-plane thermal conductivity shows strong anisotropy, i.e., κ_b is much higher than κ_a and the anisotropy ratio, κ_b / κ_a , is almost constant at 1.8 over the temperature range of 300 ~ 800 K. This is quite unconventional because PdSe₂ has nearly-uniform structure along the crystallographic axis, i.e. nearly equal in-plane lattice constants, Pd-Se bond lengths, bond strengths and the bond force constants, but shows so strong in-plane anisotropic lattice thermal conductivity. This anisotropy ratio is quite large and comparable to some of the values in the most in-plane anisotropic layered materials, such as 1.6 for black phosphorus [7], 1.4 for ReS₂ [34], 1.3 for graphene nanoribbon [6], and even comparable to the highest score of 2.0 for TiS₃ up to date [9]. Table 1 lists the anisotropy of IPTC in the materials shown in Fig. 3b, which shows the unique anisotropy in IPTC of PdSe₂, i.e., high IPTC anisotropy with nearly-equal in-plane lattice constants and the nearly-isotropic bonding. This is completely different from the cases in ReS₂ and TiS₃, where the difference between the weak bonding and the covalent bonding directions induces the IPTC anisotropy, or the case in the uniform graphene, where the IPTC anisotropy originates from the difference between the zigzag- and armchair-directions.

Table 1. Anisotropic information of various 2D layered materials at room temperature. The lattice ratios of GNR, b-P, and b-As are defined by the structure geometry.

Materials	In-plane directions		Lattice ratios	IPTC (W/mK)		IPTC ratios
				<i>a</i> -axis	<i>b</i> -axis	
PdSe ₂	<i>a</i> -axis	<i>b</i> -axis	0.98	17.45	30.70	1.79 this work
				10.95	15.58	1.42 Exp. ^a
TiS ₃	<i>a</i> -axis	<i>b</i> -axis	0.69	2.84	5.78	2.04 Exp. ^b
ReS ₂	<i>a</i> -axis	<i>b</i> -axis	0.98	50	70	1.40 Exp. ^c
Td-WTe	<i>a</i> -axis	<i>b</i> -axis	0.56	0.74	0.64	1.16 Exp. ^d
SnSe	<i>c</i> -axis	<i>b</i> -axis	0.93	0.68	0.70	1.04 Exp. ^e
GNR	zigzag	armchair	0.87	1300	1700	1.29 Cal. ^f
				(armchair)	(zigzag)	
b-P	zigzag	armchair	0.71	13.5	19.0	1.41 Exp. ^g
				(armchair)	(zigzag)	
b-As	zigzag	armchair	0.87	3.4	5.5	1.61 Exp. ^h
				(armchair)	(zigzag)	

Refs.: ^a [22], ^b [9], ^c [34], ^d [32], ^e [8], ^f [6], ^g [7], ^h [33]

It should be mentioned that our calculation shows a moderate difference with previous measurement in PdSe₂, where an anisotropy ratio of IPTC up to 1.42 in the thin flake was reported [22]. There may be two reasons for this discrepancy: (1) The thermal transport calculation is based on ideal crystal rather than a thin flake. (As a comparison, a bulk single crystal sample was used for IXS experiment.) For materials with moderate thermal conductivity and good crystalline quality/large single crystal size, the contribution from phonon-boundary and phonon-defect scattering is small. Thus, the phonon-boundary and phonon-defect scattering are weak at high temperature and was ignored in our calculations, where phonon-phonon scattering is the dominated mechanism. (2) Some limitations for micro-Raman technique, for example, the nonequilibrium phonons and temperature and strain effects are unavoidable, which may lead to inaccurate results [35,36].

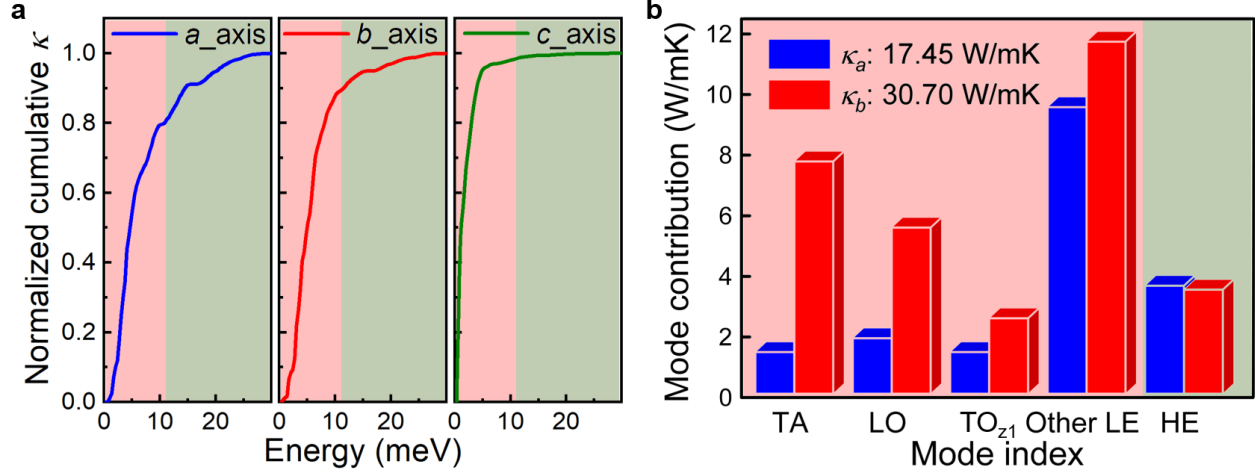


Fig. 4 Contributions to the anisotropic lattice thermal conductivity of PdSe₂. **a** Phonon energy-dependence of the anisotropic cumulative lattice thermal conductivity at 300 K. The κ is normalized with the thermal conductivity along the corresponding crystallographic direction at 300 K. **b** Mode contribution to thermal conductivity along a - and b -axis. Light-pink and dark-sea-green shadows represent the low-energy (LE)- and high-energy (HE)-phonons, respectively.

In order to explore the origin of the strong anisotropy in IPTC, the energy-dependent anisotropic cumulative lattice thermal conductivities of PdSe₂ at 300 K are shown in Fig. 4a. It is found that along a - and b -axis, the LE-phonons below 11 meV dominate the thermal conductivities by accounting for 85% of the contribution, while the high-energy (HE, 11–32 meV) optical phonons are responsible for the rest. Therefore, the main contribution to the anisotropy of the IPTC is from the LE-phonons. To further distinguish the role of phonons in the anisotropic IPTC, we calculated the mode contributions on the thermal conductivity (Supplementary Fig. 4) and selected the specific mode contribution with the main contribution ($\kappa > 2$ W/mK) to the anisotropic IPTC, as shown in Fig. 4b. Interestingly, TA, LO, and TO₂₁ branches have significantly greater values along b -axis, and respectively possess the anisotropy ratios of 5.57, 2.99, and 1.85, making them the main contribution to the anisotropic IPTC in PdSe₂. Such high

anisotropy is in excellent consistent with the phonon dispersion difference for these three branches. Other LE-phonons have a lower total anisotropic ratio of 1.23, while HE-phonons have a comparable value along the two high-symmetry directions due to the flat dispersions.

We then explore the origin of such strong anisotropy of in-plane thermal conductivity in this nearly-uniform structured material. We investigate the group velocity first since it directly contributes to the anisotropy of thermal conductivity as [37]

$$\kappa_{\alpha\beta} = \frac{1}{3} \sum_{\lambda} c_{\lambda} v_{\lambda}^{\alpha} v_{\lambda}^{\beta} \tau_{\lambda} \quad (1)$$

where c_{λ} is the specific heat capacity of phonon mode λ , $v_{\lambda}^{\alpha(\beta)}$ is the group velocity of phonon mode λ along the α (β) direction, and τ_{λ} is relaxation time of phonon mode λ . The significant in-plane phonon dispersion differences result in the high anisotropy in phonon group velocities. In order to further evaluate the anisotropy of the group velocities of all phonon branches, we calculated the energy-dependent average group velocity as [38]

$$v(\omega) = \frac{(v^{\mu})^2}{|v|}(\omega) = \left(\frac{\square \mathbf{q}}{2\pi} \right)^3 \sum_{\lambda} \frac{(v_{\lambda}^{\mu})^2}{|v_{\lambda}^{\mu}|} \delta(\omega - \omega_{\lambda}) / \sum_j g_j(\omega) \quad (2)$$

where v_{λ}^{μ} is the group velocity of phonon mode λ at wavevector \mathbf{q} along the μ -axis and $g_j(\omega)$ is the phonon density of state of mode j .

As expected, the group velocities along Γ -Y are significantly higher than that along Γ -X in the energy range from 5 to 11 meV (Fig. 5a). Since the anisotropic IPTC is mostly from TA, LO, and TO_{z1} as shown in Fig. 4b, we then investigate the group velocity of these three phonon branches along a - and b -axis directions, as shown in Figs. 5b, 5c, and Supplementary Fig. 5. It can be seen that our calculation shows good agreement with the IXS measurement at $\mathbf{q} = 0.1$.

Both the \mathbf{q} - and energy-dependent TA mode shows the large difference. Specifically, the group velocity v_{TA} exhibits a knee point along Γ -X due to the avoided-crossing behavior and thus has a much lower value beyond $\mathbf{q} > 0.2$, which contributes mostly to the strong anisotropy ratio of the in-plane thermal conductivity. Two optical branches LO and TO_{z1} , also showing large differences in group velocity, significantly contribute to this anisotropic thermal conductivity. Other LE-phonon branches have much lower contributions to this anisotropic thermal conductivity due to the small group velocity difference along a - and b -axis directions (Supplementary Fig. 5). Thus, the high group velocity difference in the TA, LO, and TO_{z1} modes dominate the high anisotropy in IPTC of $PdSe_2$.

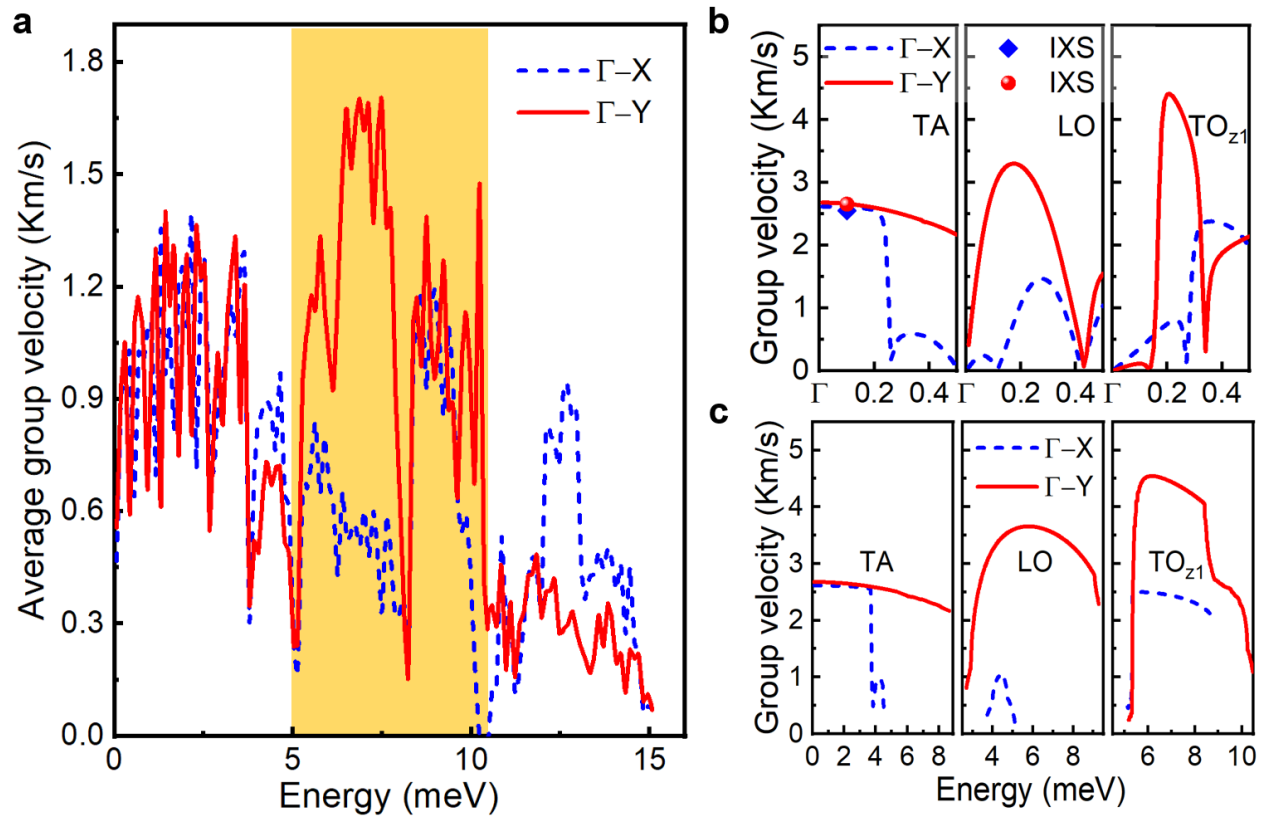


Fig. 5 Phonon group velocities of $PdSe_2$ along Γ -X and Γ -Y directions. **a** Energy-dependent average group velocity of phonon modes along Γ -X and Γ -Y, showing high anisotropy for

phonons between 5 and 10 meV. Yellow shadow is the guide for eyes. **b** and **c**, **q**-and energy-dependent absolute values of phonon group velocities of the transverse acoustic (TA) mode, longitudinal optical (LO) mode, and the first transverse optical mode vibrating along *c*-axis (TO_{z1}) along Γ -X and Γ -Y. Balls are the velocities extracted from inelastic X-ray scattering (IXS) at $\mathbf{q} = 0.1$ (r.l.u.).

The effect of the phonon scattering rate on the anisotropic IPTC is also taken into account, as shown in Fig. 6. The phonon linewidths, inversely related to the phonon relaxation time ($2\Gamma = \tau^{-1}$) [39,40], were extracted from IXS data after deconvoluting with the instrument resolution by Gaussian fitting. It can be seen that the calculated anharmonic scattering rates of the LE-phonons are smaller than those from experiments due to the neglect of other scattering processes in calculations (Fig. 6a), such as the phonon-defect scattering, phonon-interface scattering, and phonon-boundary scattering. However, the mismatch between the measurement and calculation has little impact on our discussion because the scattering terms are relatively low compared to the large difference in group velocity, i.e., the scattering rates of the LE-phonons are weak, compared to other strong anharmonic materials, such as SnSe, PbTe, and Pd_2Se_3 [41]. Although there still exists slight differences of scattering rates between Γ -X and Γ -Y directions (Figs. 6c and 6d), the scattering rates of LE-phonons are relatively low. On the other hand, they are much lower than those of HE-phonons (Fig. 6b), making them unimportant to affect the thermal conductivity in PdSe_2 . In addition, the near-quadratic properties of the frozen phonon potentials also indicate weak anharmonicity of the LE-phonons (Supplementary Fig. 6). Therefore, the low linewidths of harmonic LE-phonons have little impact on the IPTC.

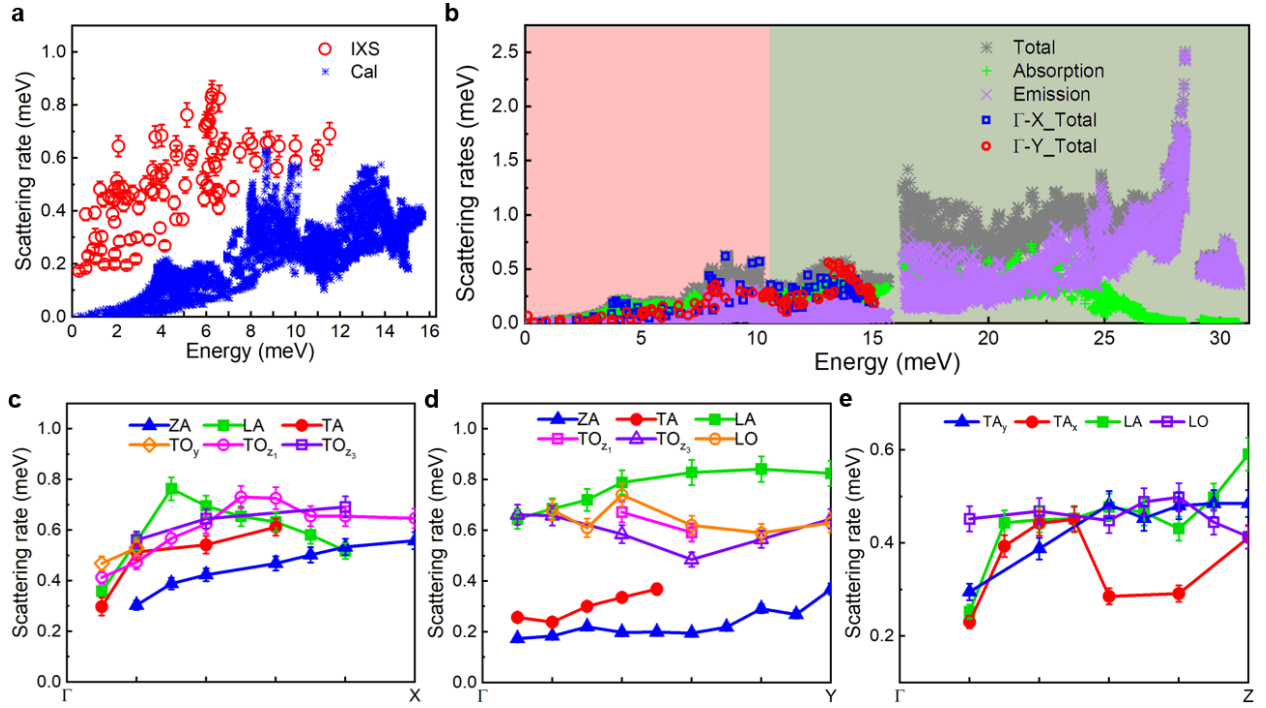


Fig. 6 Phonon scattering rates in layered PdSe₂. **a** Comparison between the experimental (inelastic X-ray scattering, IXS) and calculated (Cal) energy-dependent scattering rates. **b** Calculated energy-dependent phonon scattering rates. Light-pink and dark-sea-green shadows represent the low-energy (LE)- and high-energy (HE)-phonons, respectively. Blue hollow square and red hollow circle represent the IXS data. **c**, **d**, and **e** q -dependent scattering rates extracted from IXS data along Γ -X, Γ -Y, and Γ -Z, respectively. Blue triangle, red circle, green square, orange hollow diamond, magenta hollow circle, and purple hollow square represent the flexural acoustic (ZA) mode, transverse acoustic (TA) mode, longitudinal acoustic (LA) mode, transverse optical mode vibrating along b -axis (TO_y), the first transverse optical mode vibrating along c -axis (TO_{z1}), and the third transverse optical mode vibrating along c -axis (TO_{z3}) in **c**. Blue triangle, red circle, green square, orange hollow circle, magenta hollow square, and purple hollow triangle represent the ZA, TA, LA, longitudinal optical (LO), TO_{z1} , and TO_{z3} modes in **d**. Blue triangle, red circle, green square, and purple hollow circle represent the transverse acoustic

mode vibrating along b -axis (TA_y), transverse acoustic mode vibrating along a -axis (TA_x), LA mode, and LO mode in e . Error bars are the Gaussian fitting uncertainty.

As discussed above, the avoided-crossing behavior, mainly attributed to the structure geometry [30,31,42,43] and the unique buckling structure of $PdSe_2$, is significant for lowering the group velocities of TA and TO_{z1} branches along a -axis. Since the buckling structure induces varying levels of axial deviation of atomic vibrations, the phonon dispersions are quite different along the two in-plane high-symmetry directions [27-29]. In $PdSe_2$, the vibration of the LE-phonons has comparable displacements of heavier Pd and lighter Se atoms, especially for TA, LO, and TO_{z1} mode (Supplementary Figs. 7-9). The deviations of Pd and Se atoms from the pure longitudinal or transverse directions exist from zone center to zone boundary, leading to the large anisotropy of dispersions along zigzag- and flat-type chains. Except for the ZA branch, LO is another typical example showing the dispersion anisotropy caused by the buckling structure. Intuitively, the atomic vibration along the flat-type chain is similar to the slide motion, while the atomic vibration along the zigzag-type chain behaves the opposite motion, which undergoes large resistance. Thus, the thermal conductivity is higher along b -axis than a -axis (Supplementary Fig. 8).

Table II. Mode force constants ($meV/\text{\AA}^2$) of TA, LO, and TO_{z1} modes at $\mathbf{q} = 0$ and 0.3 along the two high-symmetry directions, obtained by the second derivation of the frozen phonon potentials. Pd_i ($i = a, b, c$) presented here as the reference of the atomic displacement in each mode.

Mode	TA	LO	TO_{z1}
------	----	----	-----------

\mathbf{q}	Γ -X	Γ -Y	Γ -X	Γ -Y	Γ -X	Γ -Y
Γ -point	Pd_b	Pd_a	Pd_a	Pd_b	Pd_c	Pd_c
	—	—	320	170	260	260
0.3	Pd_{bc}	Pd_a	Pd_{ac}	Pd_{bc}	Pd_b	Pd_b
	134	217	320	410	270	370

Here, the mode force constant (MFC), which is obtained by extracting the second derivative of frozen phonon potentials in Supplementary Fig. 6, is used to briefly explain the effect of the buckling structure in PdSe₂. MFC reflects all the atomic vibration information in a specific phonon mode, including the effect of the buckling atoms in a particular mode for the selected momentum, and thus can evaluate the “strength” of the vibration of the phonon mode. Table II lists the MFCs of the high anisotropic phonon branches TA, LO, and TO_{z1} modes at $\mathbf{q} = 0$ and 0.3 along a - and b -axis. It is found that the vibration direction of Pd atoms changes with \mathbf{q} , and the MFC shows higher values along Γ -Y than Γ -X at $\mathbf{q} = 0.3$. The anisotropy ratios for TA, LO, and TO_{z1} mode are 1.6, 1.3, and 1.4, respectively, responsible for the difference in group velocities along these two high symmetry directions.

3. Conclusion

In summary, a giant IPTC anisotropy with a ratio of about 1.8 is discovered in the pentagonal structure PdSe₂. Unlike the most layered materials where the IPTC anisotropy originates from the anisotropic structures, our findings show that the IPTC anisotropy in PdSe₂ emerges in the nearly-uniform in-plane structure with nearly-isotropic bonding. The IXS measurements show a

significant difference in the LE-phonon dispersions and the group velocities between along a - and b -axis directions, further revealed by the first-principles calculations. The lower group velocities and the avoided-crossing behaviors along Γ -X, which is induced by the puckered Se and Pd atoms in the zigzag-type chain, strongly suppress the lattice thermal conductivity along a -axis. Our results reveal a new mechanism for anisotropic IPTC in the nearly-uniform structures with nearly-isotropic bonding in 2D-layered materials and provide a theoretical basis for finding relatively high symmetry in-plane structural materials with anisotropic thermal conductivity, which are very promising for future thermal applications in novel electronic devices, such as thermal diode, modulator, or waveguide, to confine the heat to flow at a particular direction.

4. Methods

4.1 Sample information

2D-layered PdSe₂ crystal in this work was purchased commercially, which were grown by the chemical vapor transport method [44]. High purity Pd and Se powders were weighted out in stoichiometric ratio of PdSe₂, and then they were loaded into quartz tubes under vacuum. The tubes were slowly heated to 1073 K and soaked at this temperature over 100 h for fully melting and decomposing the powders. Then, the furnace was cooled to 923 K to make the gas depositing into crystals for 150 h, followed by cooling down to room temperature. The microscopic structure and the related properties could be found in Ref. [44]. The quality of the single crystal was re-checked before the IXS experiment by X-ray diffraction shown in Supplementary Fig. 1. The full width at half maximum (FWHM) of the X-ray diffraction peak at (002) plane is $0.24 \pm 0.01^\circ$, indicating the high quality of the single crystal for IXS measurement.

4.2 Inelastic X-ray scattering

The LE-phonon dispersions were measured at room temperature by IXS experiment conducted at 30-ID-C (the High-resolution Inelastic X-ray Scattering beamline, HERIX) at the Advanced Photon Source (APS). A single crystal of PdSe₂ with 60 μm thickness was attached to a copper post by varnish (inset in Supplementary Fig. 1). The incident photon energy was 23.7 keV with an energy resolution ΔE of 1.2 meV. The IXS measurements were accomplished at constant wavevector mode in transmission geometry. The orientation matrix was defined by using Bragg peaks at (2 0 0), (0 2 0), and (0 0 2).

4.3 First-principles calculations

First-principles calculations were performed based on the density functional theory (DFT) in the projector-augmented wave (PAW) [45] framework as implemented in the Vienna Ab Initio Simulation Package (VASP) [46]. The generalized gradient approximation (GGA) of Perdew-Burke-Ernzerhof (PBE) to the exchange-correlation functional was used, and the energy cut-off of 600 eV was set for the plane-wave basis. We used optPBE functional [47] to evaluate the vdW force for the layered structure PdSe₂. The Brillouin zone of the reciprocal space was sampled by a Γ -centered grid of $5 \times 5 \times 4$. The force components of each atom are smaller than 0.001 eV/Å, and the difference of total energy is less than 10^{-6} eV during the relaxation of atomic positions. The experimental lattice constants were used in the calculation, where $a = 5.741$ Å, $b = 5.868$ Å, and $c = 7.705$ Å. The Phonopy code [48] was used to calculate the phonon dispersion of layered PdSe₂. In the approach, the second-order interatomic force constants (IFCs) were computed by the finite difference method in a $2 \times 2 \times 2$ supercell. The phonon transport properties were obtained by solving the phonon Boltzmann transport equation (BTE) implemented in the ShengBTE package [49]. The fourth-nearest neighbor interactions were

considered to capture the basic phonon scattering processes embedded in this software to calculate the anharmonic IFC.

Data availability

All data needed to evaluate the conclusions in the paper are present in the paper and/or the Supplementary Information. Additional data related to this paper may be requested from the authors.

Declaration of competing interest

The authors declare that they have no known competing financial interests or personal relationships that could have appeared influence the work reported in this paper.

Acknowledgements

The work at Beijing Institute of Technology is supported by the National Key R&D Program of China (2021YFA1400300), the National Natural Science Foundation of China (Grant No. 12172047) and Beijing Natural Science Foundation (Grant No. Z190011). The work at Henan Polytechnic University is supported by the Doctoral Foundation of Henan Polytechnic University (Natural Science). Chen Li thanks the Initial Complement of University of California, Riverside. This research used the resource of the Advanced Photon Source, a US Department of Energy (DOE) Office of Science User Facility, operated for the DOE Office of Science by Argonne National Laboratory under Contract No. DE-AC02-06CH11357. Theoretical calculations were performed using resources of the National Supercomputer Centre in Guangzhou.

Author Contributions

BW and JH conceived this project and designed the experiments. BW, QC, and AHS performed the inelastic X-ray scattering measurements. JL and BW performed the theoretical calculations. BW, QC, JL, MH, JH, and CL discussed the data. BW wrote the manuscript. All authors contributed to discussing the data and editing the manuscript.

Credit statement

Bin Wei: Conceptualization, Data curation, Formal analysis, Investigation, Methodology, Project administration, Visualization, Writing original draft. Junyan Liu: Formal analysis, Investigation, Methodology, Visualization, Editing. Qingan Cai: Formal analysis, Investigation, Methodology, Validation. Ahmet Alatas: Investigation, Resources, Writing – review & editing. Ayman H. said: Investigation, Resources, Writing – review & editing. Meihua Hu: Formal analysis, Investigation, Writing – review & editing. Chen Li: Conceptualization, Funding acquisition, Investigation, Project administration, Supervision, Writing – review & editing. Jiawang Hong: Conceptualization, Funding acquisition, Investigation, Project administration, Resources, Supervision, Writing –review & editing.

Reference:

- [1] A.H.C. Neto, F. Guinea, N.M.R. Peres, K.S. Novoselov, A.K. Geim, The electronic properties of graphene, *Rev. Mod. Phys.* 81 (2009) 109-162.
- [2] K.S. Novoselov, A. Mishchenko, A. Carvalho, A.H.C. Neto, 2D materials and van der Waals heterostructures. *Science* 353 (2016) 6298.
- [3] C. Kim, J.C. Park, S.Y. Choi, Y. Kim, S.Y. Seo, T.E. Park, J.H. Ahn, Self-formed channel devices based on vertically grown 2D materials with large-surface-area and their potential for chemical sensor applications, *Small* 14 (2018) e1704116.
- [4] S. Goossens, G. Navickaite, C. Monasterio, S. Gupta, J.J. Piqueras, R. Pérez, G. Burwell, I. Nikitskiy, T. Lasanta, T. Galán, E. Puma, A. Centeno, A. Pesquera, A. Zurutuza, G. Konstantatos, F. Koppens, Broadband image sensor array based on graphene-CMOS integration, *Nat. Photonics* 11 (2017) 366-371.

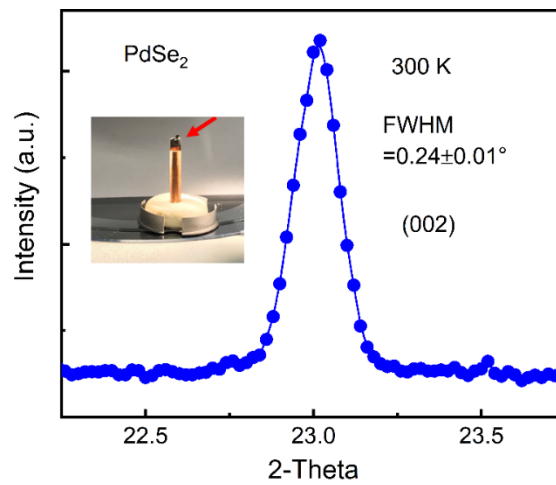
- [5] D. Pesin, A.H. MacDonald, Spintronics and pseudospintronics in graphene and topological insulators, *Nat. Mater* 11 (2012) 409-416.
- [6] J. Hu, X. Ruan, Y.P. Chen, Thermal conductivity and thermal rectification in graphene nanoribbons: a molecular dynamics study. *Nano Lett.* 9 (2009) 2730–2735.
- [7] S. Lee, F. Yang, J. Suh, S. Yang, Y. Lee, G. Li, H.S. Choe, A. Suslu, Y. Chen, C. Ko, J. Park, K. Liu, J. Li, K. Hippalgaonkar, J.J. Urban, S. Tongay, J. Wu, Anisotropic in-plane thermal conductivity of black phosphorus nanoribbons at temperatures higher than 100 K, *Nat. Commun.* 6 (2015) 8573.
- [8] L.D. Zhao, S.H. Lo, Y. Zhang, H. Sun, G. Tan, C. Uher, C. Wolverton, V.P. Dravid, M.G. Kanatzidis, Ultralow thermal conductivity and high thermoelectric figure of merit in SnSe crystals, *Nature* 508 (2014) 373–377..
- [9] H. Liu, X. Yu, K. Wu, Y. Gao, S. Tongay, A. Javey, L. Chen, J. Hong, J. Wu, Extreme in-plane thermal conductivity anisotropy in titanium trisulfide caused by heat-carrying optical phonons, *Nano Lett.* 20 (2020) 5221-5227.
- [10] G. Qin, Q.B. Yan, Z. Qin, S.Y. Yue, M. Hu, G. Su, Anisotropic intrinsic lattice thermal conductivity of phosphorene from first principles. *Phys. Chem. Chem. Phys.* 17(7) (2015) 4854-4858.
- [11] Y. Hong, J. Zhang, X. Huang, X.C. Zeng, Thermal conductivity of a two-dimensional phosphorene sheet: a comparative study with graphene. *Nanoscale* 7(44) (2015) 18716-18724.
- [12] C. Zhang, X.L. Hao, C.X. Wang, N. Wei, T. Rabczuk, Thermal conductivity of graphene nanoribbons under shear deformation: A molecular dynamics simulation. *Sci. Rep.* 7(1) (2017) 1-8.
- [13] S. Zhang, J. Zhou, Q. Wang, X. Chen, Y. Kawazoe, P. Jena, Penta-graphene: A new carbon allotrope, *P. Natl. Acad. Sci. USA.* 112 (2015) 2372-2377.
- [14] Y. Aierken, O. Leenaerts, F.M. Peeters, A first-principles study of stable few-layer penta-silicene, *Phys. Chem. Chem. Phys.* 18 (2016) 18486-18492.
- [15] S. Deng, L. Li, Y. Zhang, Strain modulated electronic, mechanical, and optical properties of the monolayer PdS₂, PdSe₂, and PtSe₂ for tunable devices, *ACS Appl. Nano Mater.* 1 (2018) 1932-1939.
- [16] F. Xiao, W. Lei, W. Wang, L. Xu, S. Zhang, X. Ming, Pentagonal two-dimensional noble-metal dichalcogenides PdSSe for photocatalytic water splitting with pronounced optical absorption and ultrahigh anisotropic carrier mobility, *J. Mater. Chem. C* 9 (2021) 7753-7764.
- [17] W. Lei, B. Cai, H. Zhou, G. Heymann, X. Tang, S. Zhang, X. Ming, Ferroelastic lattice rotation and band-gap engineering in quasi 2D layered-structure PdSe₂ under uniaxial stress, *Nanoscale*, 11 (2019) 12317-12325.
- [18] Q. Liang, Q. Wang, Q. Zhang, J. Wei, S.X. Lim, R. Zhu, J. Hu, W. Wei, C. Lee, C. Sow, W. Zhang, A.T.S Wee, High-performance, room temperature, ultra-broadband photodetectors based on air-stable PdSe₂, *Adv. Mater.* 31 (2019) 1807609.
- [19] Q. Liang, Q. Wang, Q. Zhang, J. Wei, S.X. Lim, R. Zhu, J. Hu, W. Wei, C. Lee, C. Sow, W. Zhang, A.T.S Wee, Few-layer PdSe₂ sheets: promising thermoelectric materials driven by high valley convergence, *ACS Omega* 3 (2018) 5971-5979.
- [20] A.A. Puzdov, A.D. Oyedele, K. Xiao, A.V. Haglund, B.G. Sumpter, D. Mandrus, D.B. Geohegan, L. Liang, Anomalous interlayer vibrations in strongly coupled layered PdSe₂, *2D Mater.* 5 (2018) 035016.
- [21] W. Luo, A.D. Oyedele, Y. Gu, T. Li, X. Wang, A.V. Haglund, D. Mandrus, A.A. Puzdov, K. Xiao, L. Liang, X. Ling, Anisotropic phonon response of few-layer PdSe₂ under uniaxial strain, *Adv. Funct. Mater.* 30 (2020) 2003215.
- [22] L. Chen, W. Zhang, H. Zhang, J. Chen, C. Tan, S. Yin, G. Li, Y. Zhang, P. Gong, L. Li, In-plane anisotropic thermal conductivity of low-symmetry PdSe₂, *Sustainability* 13 (2021) 4155.
- [23] C. Souillard, X. Rocquefelte, P.E. Petit, M. Evain, S. Jubic, J.P. Itié, P. Munsch, H.J. Koo, M.H. Whangbo, Experimental and theoretical investigation on the relative stability of the PdS₂- and pyrite-type structures of PdSe₂, *Inorg. Chem.* 43 (2004) 1943-1949.
- [24] P. Lv, G. Tang, Y. Liu, Y. Lun, X. Wang, J. Hong, Van der Waals direction transformation induced by shear strain in layered PdSe₂, *Extreme Mech. Lett.* 44 (2021) 101231.
- [25] L. Lindsay, D.A. Broido, N. Mingo, Flexural phonons and thermal transport in graphene, *Phys. Rev. B* 82 (2010) 115427.
- [26] H. Liu, G. Qin, Y. Lin, M. Hu, Disparate strain dependent thermal conductivity of two-dimensional penta-structures, *Nano Lett.* 16 (2016) 3831-3842.
- [27] H. Xie, T. Ouyang, É. Germaneau, G. Qin, M. Hu, H. Bao, Large tunability of lattice thermal conductivity of monolayer silicene via mechanical strain, *Phys. Rev. B* 93 (2016) 075404.
- [28] X. Zhang, H. Xie, M. Hu, H. Bao, S. Yue, G. Qin, G. Su, Thermal conductivity of silicene calculated using an optimized Stillinger-Weber potential, *Phys. Rev. B* 89 (2014) 054310.

- [29] X. Gu, R. Yang, First-principles prediction of phononic thermal conductivity of silicene: A comparison with graphene, *J. Appl. Phys.* 117 (2015) 025102.
- [30] M. Christensen, A.B. Abrahamsen, N.B. Christensen, F. Juranyi, N.H. Andersen, K. Lefmann, J. Andreasson, C.R.H. Bahl, B.B. Iversen, Avoided crossing of rattler modes in thermoelectric materials, *Nat. Mater.* 7 (2008) 811-815.
- [31] Y. Zhu, B. Wei, J. Liu, N.Z. Koocher, Y. Li, L. Hu, W. He, G. Deng, W. Xu, X. Wang, J.M. Rondinelli, L.D. Zhao, G.J. Snyder, J. Hong, Physical insights on the low lattice thermal conductivity of AgInSe₂, *Mater. Today Phys.* 19 (2021) 100428.
- [32] Y. Chen, B. Peng, C. Cong, J. Shang, L. Wu, W. Yang, J. Zhou, P. Yu, H. Zhang, Y. Wang, C. Zou, J. Zhang, S. Liu, Q. Xiong, H. Shao, Z. Liu, H. Zhang, W. Huang, T. Yu, In-plane anisotropic thermal conductivity of few-layered transition metal dichalcogenide Td-WTe₂, *Adv. Mater.* 31 (2019) 1804979.
- [33] Y. Chen, C. Chen, R. Kealhofer, H. Liu, Z. Yuan, L. Jiang, J. Suh, J. Park, C. Ko, H.S. Choe, J. Avila, M. Zhong, Z. Wei, J. Li, S. Li, H. Gao, Y. Liu, J. Analytis, Q. Xia, M.C. Asensio, J. Wu, Black arsenic: a layered semiconductor with extreme in-plane anisotropy, *Adv. Mater.* 30 (2018) 1800754.
- [34] H. Jang, C.R. Ryder, J.D. Wood, M.C. Hersam, D.G. Cahill, 3D Anisotropic thermal conductivity of exfoliated rhenium disulfide, *Adv. Mater.* 29 (2017) 1700650.
- [35] S. Huang, Y. Chen, Z. Luo, X. Xu, Temperature and Strain Effects in Micro-Raman Thermometry for Measuring In-Plane Thermal Conductivity of Thin Films, *Nanosc. Microsc. Therm.* (2021) 1-10.
- [36] J.J. Fernandez, E.C. Angel, C.M.S. Torres, Raman thermometry analysis: Modelling assumptions revisited, *Appl. Therm. Eng.* 130 (2018) 1175-1181.
- [37] D.A. Broido, M. Malorny, G. Birner, N. Mingo, D.A. Stewart, Intrinsic lattice thermal conductivity of semiconductors from first principles, *Appl. Phys. Lett.* 91 (2007) 231922.
- [38] S. Mukhopadhyay, L. Lindsay, D.J. Singh, Optic phonons and anisotropic thermal conductivity in hexagonal Ge₂Sb₂Te₅, *Sci. Rep.* 6 (2016) 37076.
- [39] B. Wei, X. Yu, C. Yang, X. Rao, X. Wang, S. Chi, X. Sun, J. Hong, Low-temperature anharmonicity and the thermal conductivity of cesium iodide, *Phys. Rev. B* 99 (2019) 184301.
- [40] B. Wei, Q. Cai, Q. Sun, Y. Su, A.H. Said, D.L. Abernathy, J. Hong, C. Li, Matryoshka phonon twinning in α -GaN, *Commun. Phys.* 4(227) (2021) 1-9.
- [41] B. Wei, Q. Sun, C. Li, and J. Hong, Phonon anharmonicity: a pertinent review of recent progress and perspective, *Sci. China-Phys. Mech. Astron.* 64 (2021) 117001.
- [42] W. Li, J. Carrete, G.K. Madsen, N. Mingo, Influence of the optical-acoustic phonon hybridization on phonon scattering and thermal conductivity, *Phys. Rev. B* 93 (2016) 205203.
- [43] M.T. Dove, *Introduction to lattice dynamics* (NO. 4), Cambridge univ. press, Cambridge, 1993.
- [44] <https://2d-material.com/>
- [45] P. E. Blöchl, Projector augmented-wave method, *Phys. Rev. B* 50 (1994) 17953.
- [46] G. Kresse, J. Furthmüller, Efficiency of ab-initio total energy calculations for metals and semiconductors using a plane-wave basis set, *Phys. Rev. B* 54 (1996) 11169; *Comput. Mater. Sci.* 6 (1996) 15-50.
- [47] J. Klimeš, D.R. Bowler, A. Michaelides, Chemical accuracy for the van der waals density functional. *J. Phys.: Condens. Matter* 22 (2009) 022201.
- [48] A. Togo, F. Oba, I. Tanaka, First-principles calculations of the ferroelastic transition between rutile-type and CaCl₂-type Si at high pressures. *Phys. Rev. B* 78 (2008) 134106.
- [49] W. Li, J. Carrete, N.A. Katcho, N. Mingo, ShengBTE: A solver of the Boltzmann transport equation for phonons, *Comput. Phys. Commun.* 185 (2014) 1747.

Supplementary information for
**Giant Anisotropic in-Plane Thermal Conduction Induced by Anomalous Phonons in
Pentagonal Structured PdSe₂**

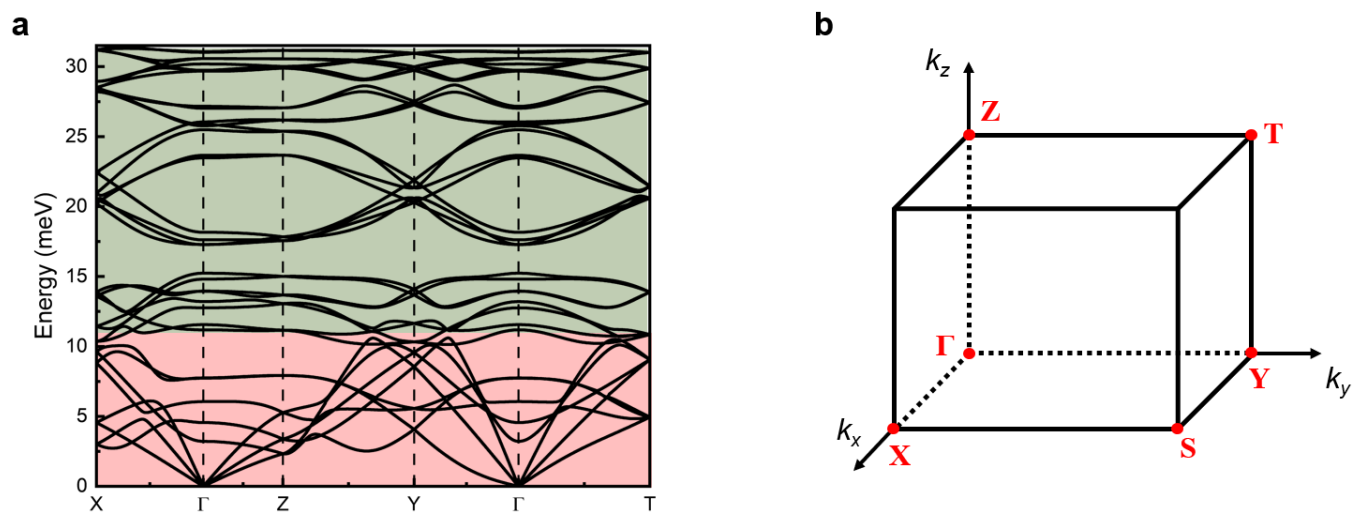
B. Wei et al

Supplementary Fig. 1 shows the sample information of PdSe₂ for IXS measurements. The narrow full-width-at-half-maximum (FWHM) indicates the high quality of the crystal.



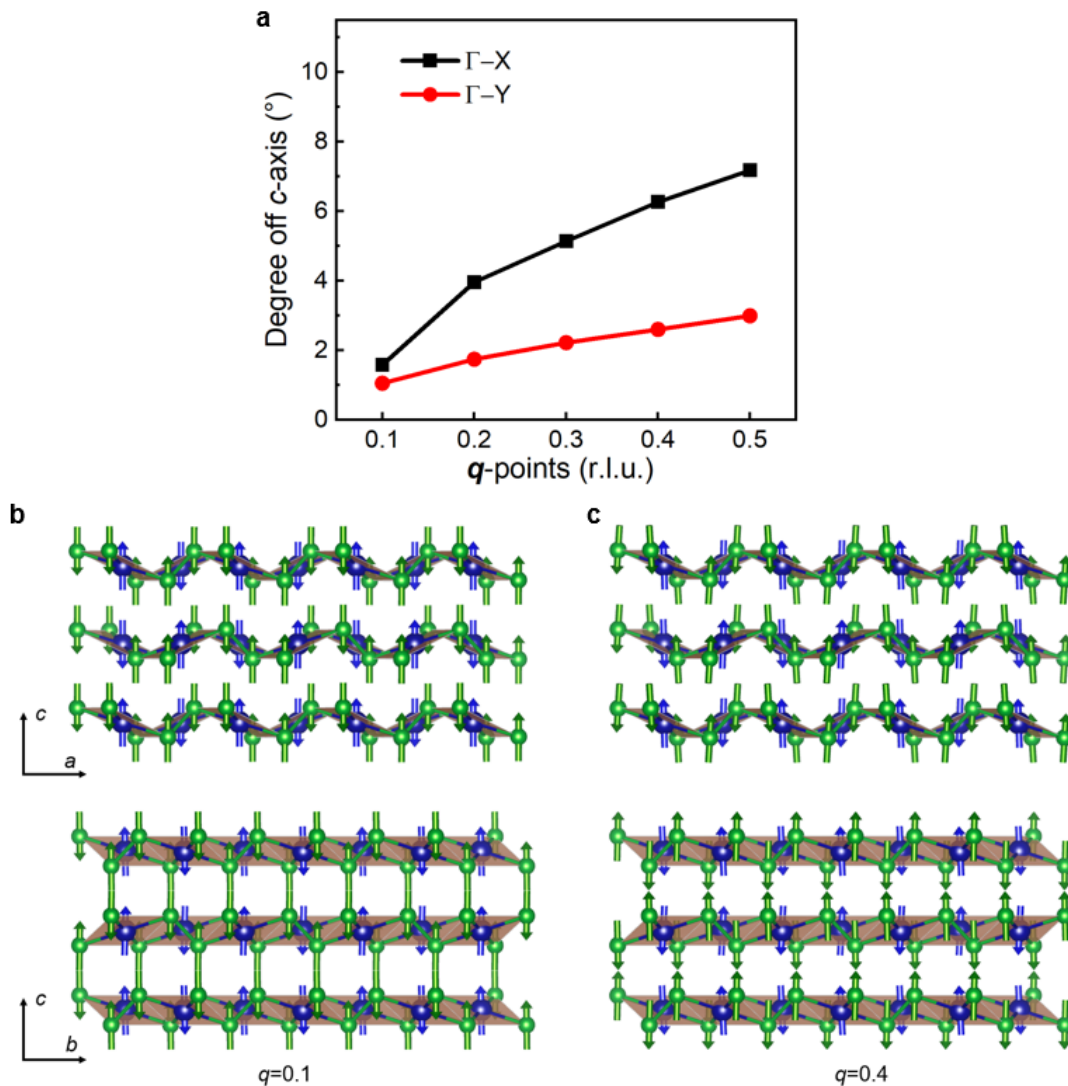
Supplementary Fig. 1 Rocking curve of PdSe₂ single crystal for Bragg peak at (002) showing the high quality of the sample. Inset is the exploited sample with 60 μm thickness attached on a copper post for IXS measurement.

Supplementary Fig. 2a shows the calculated phonon dispersions of PdSe₂ throughout the Brillouin zone (Supplementary Fig. 2b), which is sorted by three groups based on the phonon energy, i.e., the low-energy (LE) phonons (including the acoustic and LE-optical phonons) with dispersive branches, the middle-energy (ME) and the high-energy (HE) phonons with non-dispersive branches.



Supplementary Fig. 2 Entire phonon dispersion (a) and the Brillouin zone (b) of PdSe₂. Light-pink and dark-sea-green shadows represent the LE- and HE-phonons, respectively.

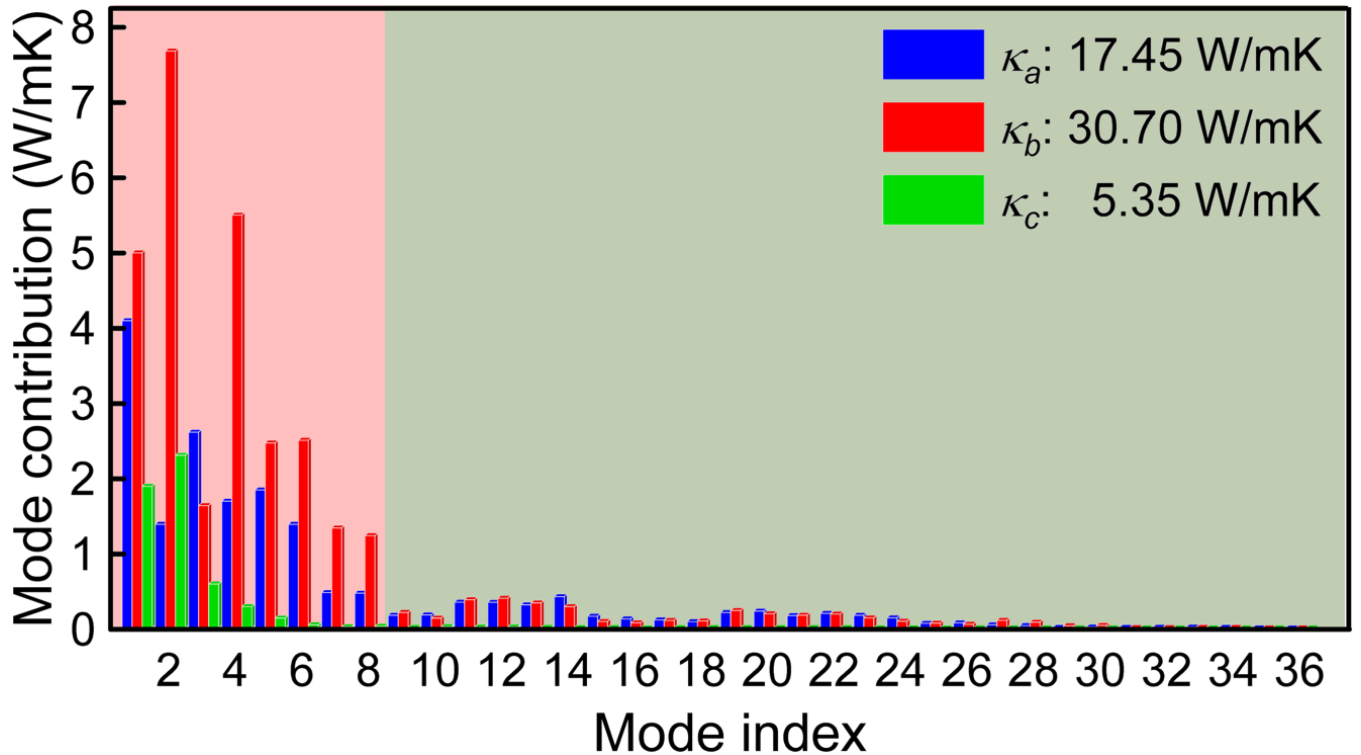
Supplementary Fig. 3a shows the degree of the derivation of the real part in ZA mode eigenvector heavier Pd atom. The larger derivation along Γ -X indicates the linear-like dispersion of ZA, while the little derivation along Γ -Y indicates a non-pure quadratic dispersion of ZA. Supplementary Figs. 3b and 3c show the vibration pattern of ZA along a - (upper) and b -axis (bottom) at $q = 0.1$ and 0.4 , respectively. It can be seen that Pd and Se atoms have similar displacements, and the derivation of the atoms from c -axis is larger along a -axis than b -axis.



Supplementary Fig. 3 Deviation of the real part of the eigenvector from c -axis of the atoms in ZA modes. **a** Degree of the derivation of Pd atoms along Γ -X and Γ -Y directions. **b** and **c** are

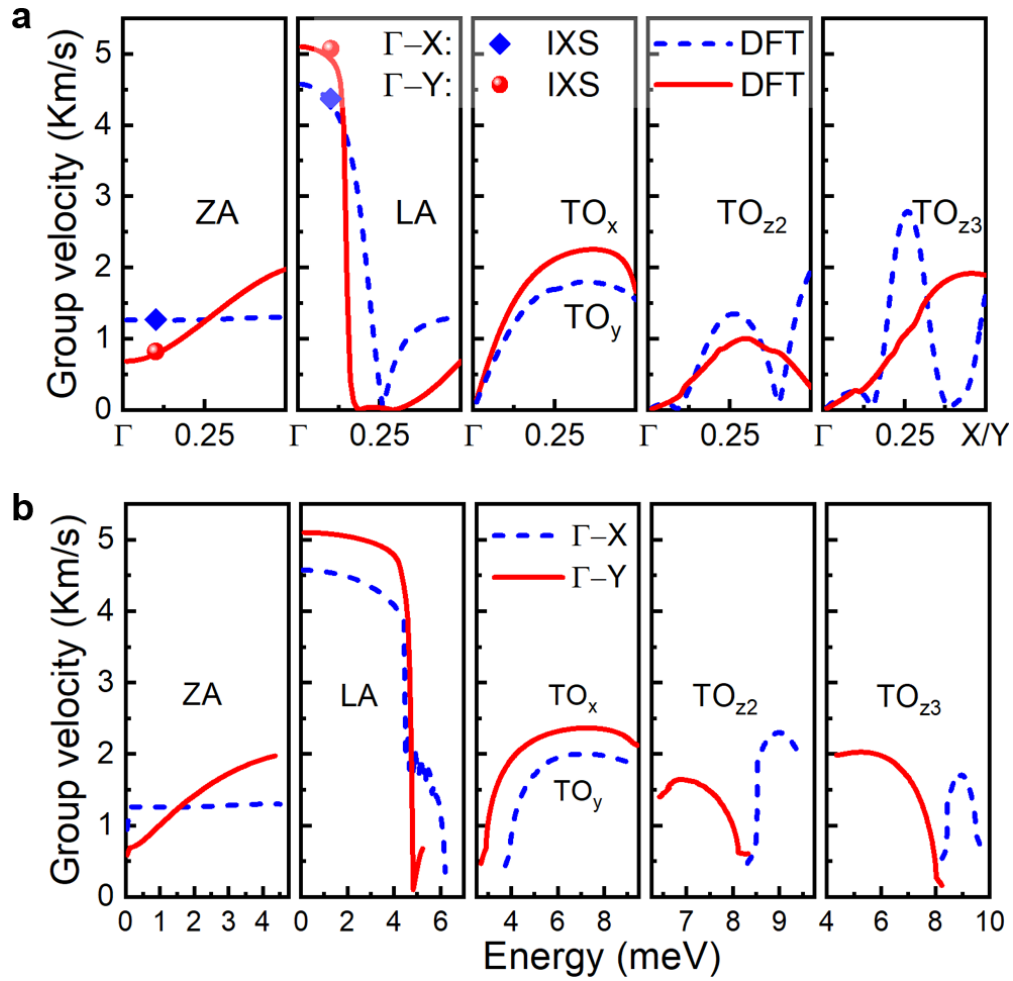
the vibration pattern of ZA mode along a - and b -axis at $\mathbf{q} = 0.1$ and 0.4 , respectively. Blue balls represent the Pd atoms, and green balls represent the Se atoms. Arrows are the displacement of each atom.

Supplementary Fig. 4 shows the difference between each mode contribution to thermal conductivity along a -, b - and c -axis. It can be seen that 1st–8th modes (LE-phonon energy region) contribute more to the thermal conductivity. The mode contributions along a - and b -axis are higher than that along c -axis due to the weak interlayer van der Waals interactions. The difference between along a - and b -axis is mainly caused by 1st–8th modes discussed in detail in the main text. In LE-phonons, TA (2nd), LO (5th mode along a -axis and 4th mode along b -axis), and TO _{z_1 - z_3} (6th–8th modes) possess higher anisotropy, which are mainly responsible for the high anisotropy of IPTC in PdSe₂.



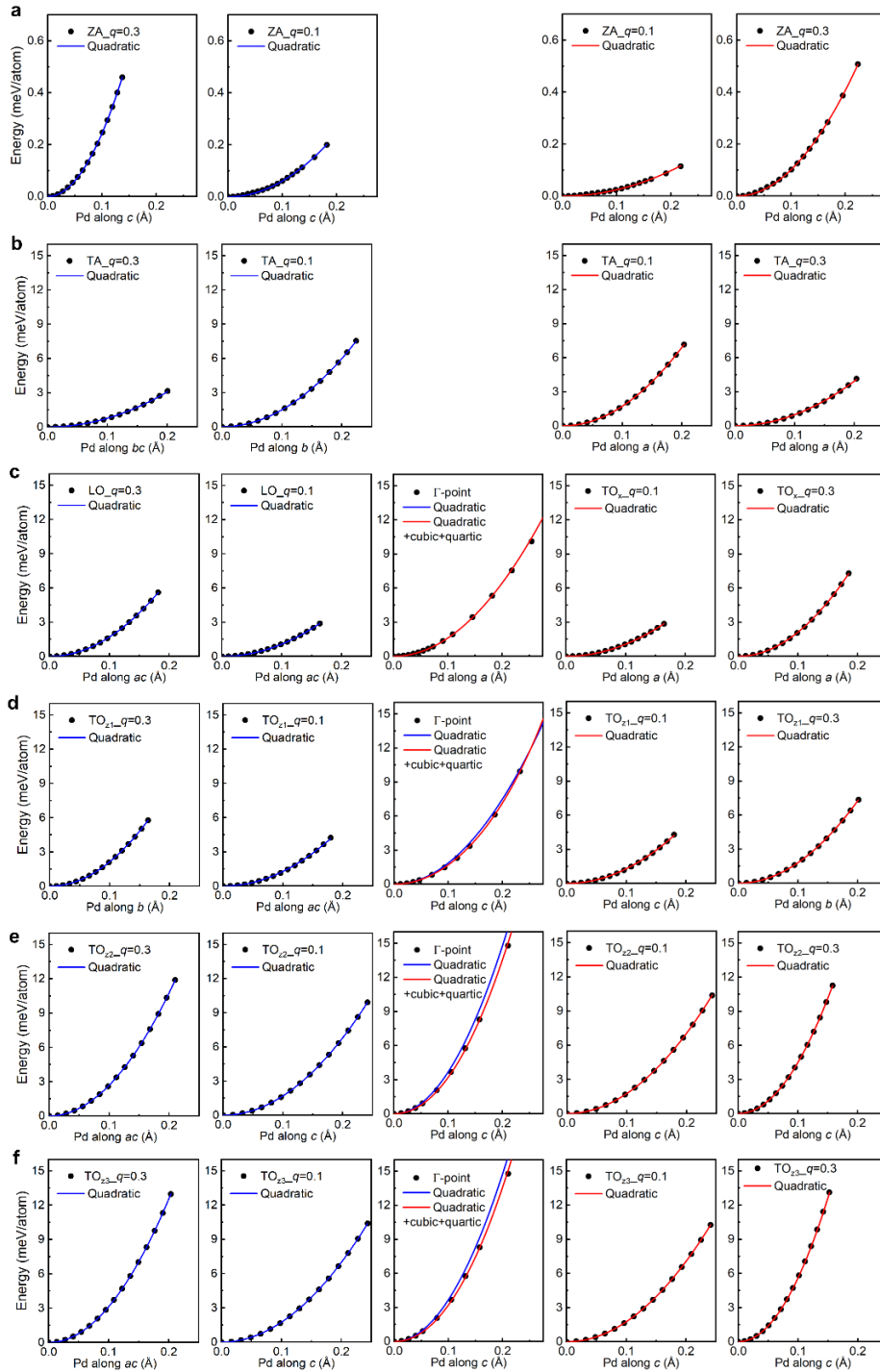
Supplementary Fig. 4 Mode contribution of each phonon branch on the thermal conductivity along a -, b -, and c -axis. Light-pink and dark-sea-green shadows represent the LE- and HE-phonons, respectively.

Supplementary Fig. 5 shows the \mathbf{q} - and energy-dependent phonon group velocities of ZA, LA, $\text{TO}_{x/y}$, TO_{z2} , and TO_{z3} branches along Γ -X and Γ -Y. The group velocity of ZA mode shows a near-constant value along Γ -X, while it monotonically increases along Γ -Y. It should be noted that ZA mode has higher group velocity along Γ -X than along Γ -Y near zone center due to its linear dispersion behavior, as confirmed by the extracted velocities from IXS measurements. LA branch has a drop due to the avoided-crossing behavior. The group velocity of TO_x has a higher value than that of TO_y over the \mathbf{q} and energy region, while the group velocities of TO_{z2} and TO_{z3} possess comparable values between the two axes directions.



Supplementary Fig. 5 q- (a) and energy-dependent (b) absolute values of phonon group velocities of ZA, LA, TO_{x/y}, TO_{z2}, and TO_{z3} branches along Γ -X and Γ -Y. Balls are the velocities extracted from IXS at $q = 0.1$ (r.l.u.).

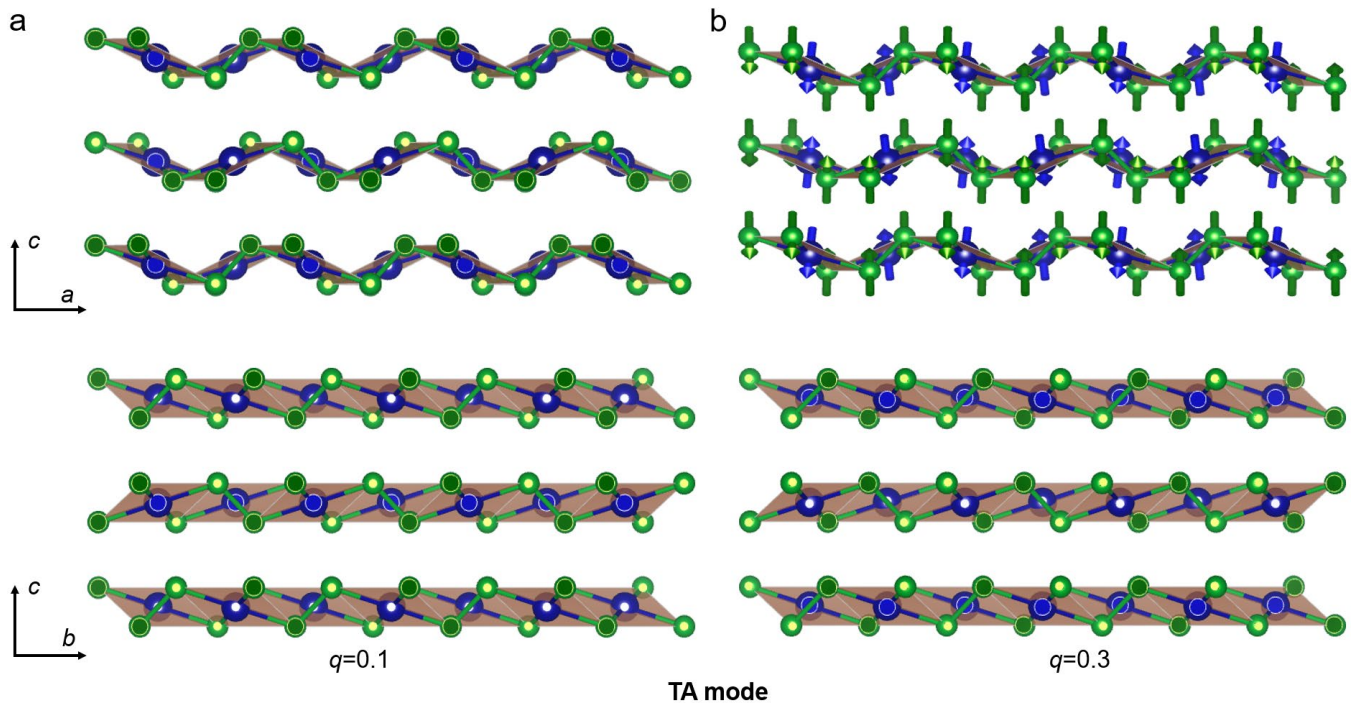
Supplementary Fig. 6 show the frozen phonon potentials of the LE-optical modes along X- Γ -Y direction. It is found that all the LE-optical modes exhibit weak anharmonicity due to the near-quadratic profile.



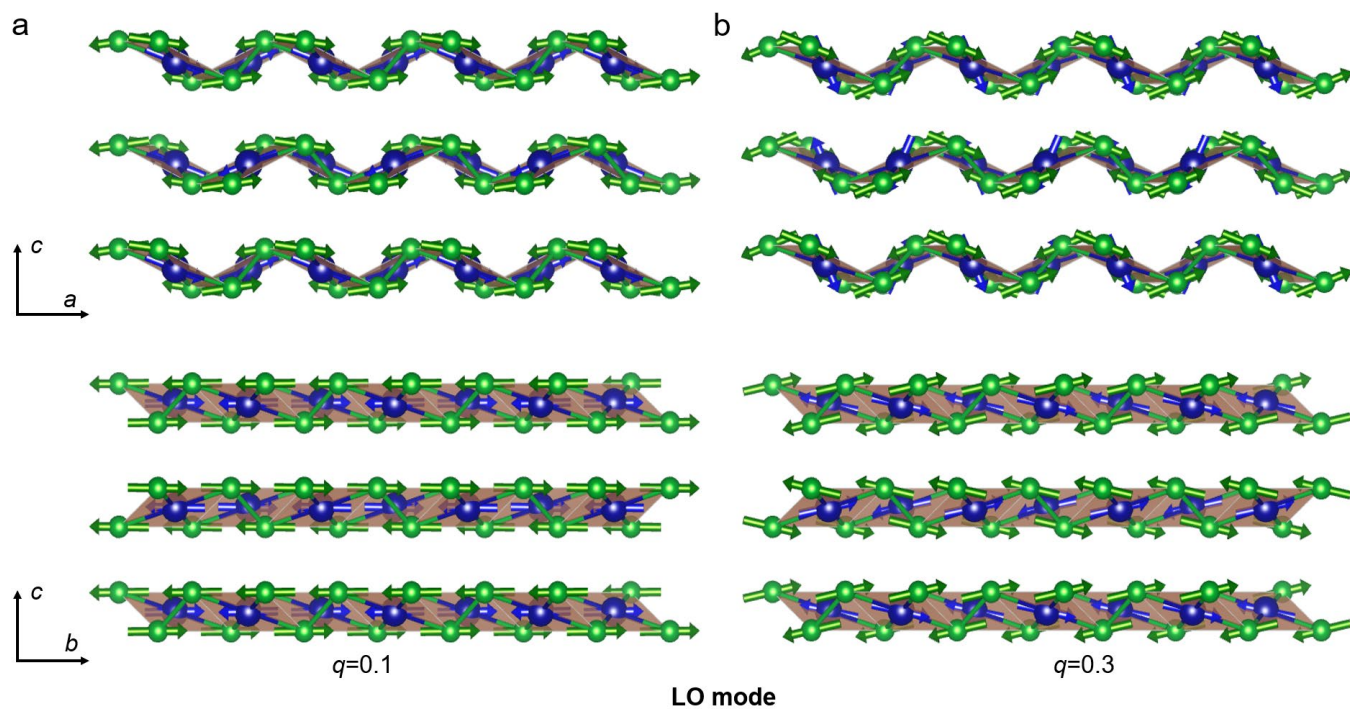
Supplementary Fig. 6 Frozen phonon potentials of the LE phonons along the q -path, indicating the harmonic behavior of these modes. a, b, c, d, and e are the potentials of the 2nd (TA), 5th (LO along Γ -X and TO_x along Γ -Y) 6th (TO_{z1}), 7th (TO_{z2}), and 8th (TO_{z3}) modes at q -points along X- Γ -Y direction from left to right, respectively. Supplementary Figs. 7-9 show the vibration patterns of TA, TO, LO, and TO_{z1} modes, respectively.

In TA, due to the avoided-crossing around $q = 0.3$ along Γ -X, there is a significant difference

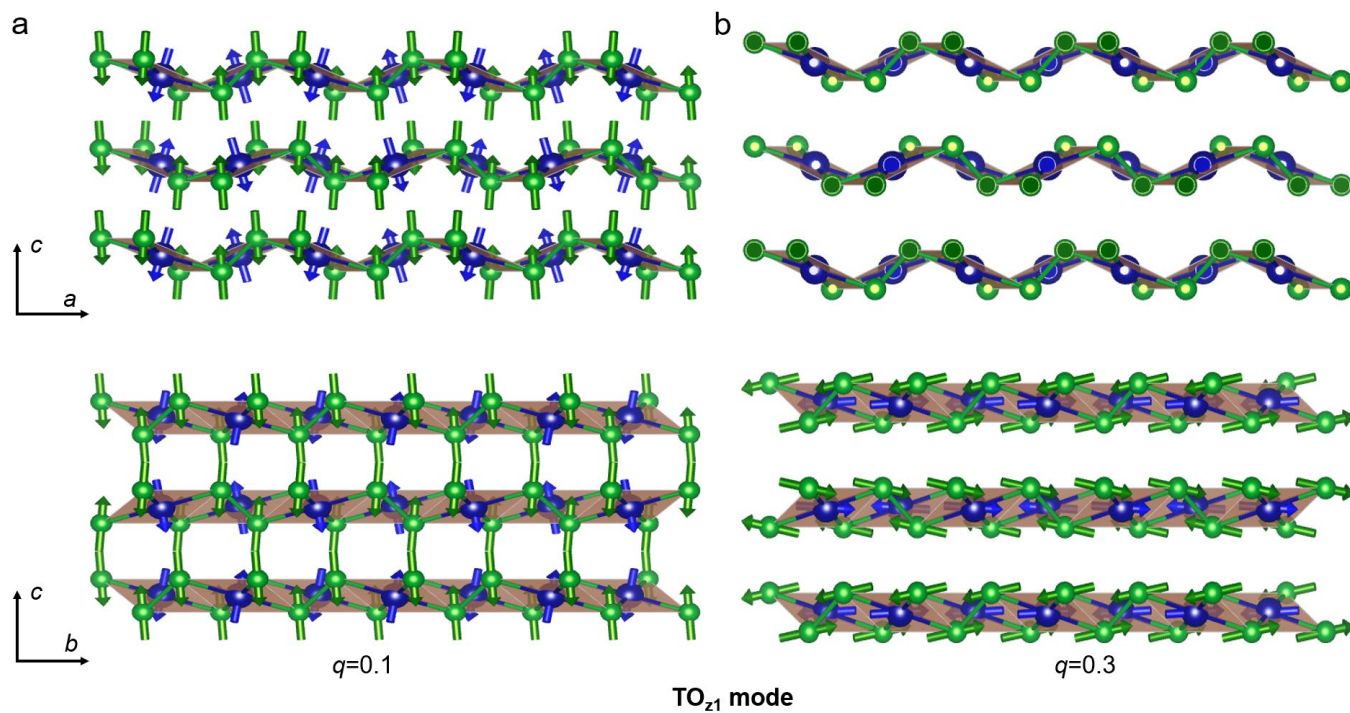
between the atomic vibrations in the zigzag and flat puckers. In LO, it is found that the atoms vibrate nearly along the zigzag edge directions along a -axis, especially at high \mathbf{q} -points, leading to a "wave-like" dispersive behavior along Γ -X. However, they vibrate nearly along b -axis, leading to a conventional dispersive mode along Γ -Y, and thus the anisotropic phonon dispersion behavior. In TO_{z1} , the atoms show a typical feature of the out-of-plane vibration mode at $\mathbf{q} = 0.1$. At $\mathbf{q} = 0.3$, due to the avoided-crossing along both Γ -X and Γ -Y, the atoms show TA vibrations in the zigzag puckers while they show LA vibrations in the flat puckers. Therefore, the bucking structure induces significant differences in phonon dispersions between Γ -X and Γ -Y.



Supplementary Fig. 7 Vibration patterns of TA mode along a - and b -axis at $\mathbf{q} = 0.1$ (a) and 0.3 (b), respectively.



Supplementary Fig. 8 Vibration patterns of LO mode along a - and b -axis at $q = 0.1$ (a) and 0.3 (b), respectively.



Supplementary Fig. 9 Vibration patterns of TO_{z1} mode along a - and b -axis at $q = 0.1$ (a) and 0.3 (b), respectively.

Supplementary Table I lists the real parts of the eigenvectors of Pd atoms in ZA mode along a - (zigzag) and b -axis (planar) directions, based on which Supplementary Fig. 3 was obtained.

Supplementary Table I. Real parts of the eigenvectors of Pd atoms along zigzag and planar directions.

q -points	Directions	Real part of the eigenvectors (Å)		
		X	Y	Z
0.1	Zigzag	-0.0013	-0.0032	0.3185
	Planar	-0.0003	-0.0058	0.3168
0.2	Zigzag	0.0031	0.0053	-0.3229
	Planar	-0.0007	0.0096	-0.3164
0.3	Zigzag	0.005	0.0059	-0.334
	Planar	0.0002	0.0123	-0.3175
0.4	Zigzag	-0.0076	-0.0053	0.3543
	Planar	0.0021	-0.0145	0.3228
0.5	Zigzag	-0.0371	0.0549	0.5261
	Planar	-0.0114	0.022	-0.4744